ESA Contract 4000114981/15/I-LG
PV-LAC

DELIVERABLES
D-2-A2 (ATBD)
D-3-A2 (IODD)

Prepared by : Y. Govaerts, M. Luffarelli and E. Pinat (Rayference)
Reference : CISAR-ATBD-V2.0
Version : V2.0
Date : October 2017

Document Change Record

Doc. Version	Date	CISAR Release	Remarks
Version 0.2	November 2016	Draft	First released version - Science Review
Version 2.0	October 2017	2.0	Final released version - Final meeting

Table of Contents

List of Acronyms

AERONET	Aerosol Robotic Network
AOT	Aerosol Optical Thickness
ATBD	Algorithm Theoretical Basis Document
AU	Astronomical Unit
BHR	BiHemispherical Reflectance
BRF	Bidirectional Reflectance Factor
CISAR	Combined Inversion of Surface and AeRosol
CMa	Cloud Mask
ECMWF	European Centre for Medium- Range Weather Forecasts
EQMPN	Equivalent Model Parameter Noise
ESA	European Space Agency
GSD	Ground Sampling Distance
IFOV	Instantaneous Field Of View
LED	Light-Emitting Diode
LSM	Land Sea Mask
LUT	Look-Up Table
MISR	Multiangle Imaging Spectro-Radiometer
MSG	Meteosat Second Generation
NIR	Near Infrared
OE	Optimal Estimation
PROBA-V	Project for On-Board Autonomy – Vegetation
RPV	Rahman - Pinty - Verstraete BRF model
RTM	Radiation Transfer Model
SWIR	Shortwave Infrared
SWS	Surface Wind Speed
TCO3	Total column Ozone
TCWV	Total Column Water Vapour
TOA	Top-Of-Atmosphere
VNIR	Visible and Near Infrared

EXECUTIVE SUMMARY

This document describes the algorithm used to generate surface reflectance and aerosol optical thickness products from PROBA-V observations. This algorithm relies on a joint retrieval of surface reflectance and aerosol optical thickness based on the inversion of a coupled surface-atmosphere radiative transfer model.

The forward model is explicitly solved during the inversion process, *i.e.*, it does not rely on precomputed solutions, allowing a continuous variations of the state variables in the solution space.

The retrieval scheme is based on an Optimal Estimation (OE) approach where the cost function accounts for the differences between the observations and the forward radiative transfer model, the retrieved state variables and their prior information and finally smoothness constraints on temporal and spectral variations of the aerosol properties.

1 INTRODUCTION

This ATBD describes the CISAR algorithm that infers surface reflectance and aerosol optical thickness over land surfaces from observations acquired by the PROBA-V radiometer in bands 0.4, 0.6, 0.8 and 1.6μm.

As the algorithm derives the total column aerosol optical thickness, it does not discriminate between tropospheric and stratospheric aerosols. This algorithm relies on a joint retrieval of surface reflectance and aerosol optical thickness based on the inversion of a coupled surface-atmosphere radiative transfer model (Govaerts and Luffarelli 2017).

The CISAR algorithm can perform the retrieval on both land and sea surface. Hence, even though for Proba-V it is applied only on land, this ATBD describes the approach for sea surfaces as well. FASTRE, the forward model included in the CISAR algorithm, is explicitly solved during the inversion process, *i.e.*, it does not rely on pre-computed solutions, allowing a continuous variation of the state variables in the solution space.

The retrieval scheme is based on an Optimal Estimation (OE) approach where the cost function accounts for the differences between the observations and the forward radiative transfer model, the retrieved state variables and their prior information and finally smoothness constraints on temporal and spectral variations of the aerosol properties.

The proposed algorithm capitalizes on the capability of PROBA-V to acquire data at least once a day over a given location to perform an angular sampling of the same radiance field under various angular geometries. The temporal accumulation of data acquired under different illumination conditions is thus used to form a virtual multi-angular measurement system. PROBA-V data are thus accumulated in the 0.4, 0.6, 0.8 and 1.6μm bands during a given period to form the measurement vector. The primary objective of this accumulation is to document the surface BRF. It is therefore performed during N_d days to minimize the effects of clouds and maximize the angular sampling of the surface BRF. During this accumulation period, surface properties are assumed temporally invariant. The inversion procedure takes place at the end of this accumulation period to retrieve the surface reflectance in each band and the Aerosol Optical Thickness (AOT) at 0.55μm.

2 INSTRUMENT CHARACTERISTICS

The PROBA-V (Project for On-Board Autonomy – Vegetation) remote-sensing satellite mission is intended to ensure the continuation of the SPOT 5 VEGETATION products after May 2014. PROBA-V flies at an altitude of 820 km. The microsatellite is designed to offer a global coverage of land surfaces at four spectral bands at a spatial resolution of 1/3km and 1km with a daily revisit for latitudes from +75°N to 56°S (Sterckx et al. 2014). To cover the wide angular field of view (101°) in a small-sized platform, the optical design of PROBA-V is made up of three cameras (identical three-mirror anastigmatic (TMA) telescopes). The three cameras have an equal field of view, the center camera pointing down covers a swath of 500km, while the right and left cameras cover 875 km each. Each camera has two focal planes, one for the short wave infrared (SWIR) band and one for the visible and near-infrared (VNIR) bands. The VNIR detector consists of four lines of 5200 pixels. Three spectral bands are selected, compatible with SPOT-VEGETATION (SPOT-VGT): blue, red, and near infrared (NIR). The SWIR detector is a linear array composed of three mechanically staggered detectors of 1024 pixels. The ground sampling distance (GSD) for the central camera is 100m in the across-track direction, while for the side cameras it varies from 300m to more than 660m at the swath edges. The SWIR imaging pixels are twice as large but result in a similar geometry: 200×200m in the centre varying to 200×600m at the edge of the side cameras. Because of the omission of on-board calibration devices, such as Light emitting Diode (LED) lamps, due to the constraints on size, weight and power consumption, the PROBA-V in-flight calibration relies only on vicarious methods.

3 FORWARD MODEL

3.1 Vertical structure

FASTRE, the forward model $y_m(\mathbf{x}, \mathbf{b}; \mathbf{m})$ simulates the TOA Bidirectional Reflectance Factor as a function of the viewing and illumination angles, the spectral band $\tilde{\lambda}$, the state of the atmosphere and underlying surface. This model depends on the retrieved state variables $\mathbf{x}$, the model parameters $\mathbf{b}$ and finally the observation conditions. The independent parameters, such as the acquisition geometry or the spectral band, that determine these observation conditions are denoted $\mathbf{m}$. The radiative transfer equation is solved with the Matrix Operator Method (Fischer and Grassl 1984) optimised by Liu and Ruprecht (1996) for a finite number of quadrature points.

The FASTRE model is designed to simulate radiometer observations acquired with a spectral interval characterized by the spectral response of the processed radiometer. The gaseous transmittance in these intervals is precomputed and stored in look-up tables. All other operations are performed online, *i.e.*, during the inversion process. The model separates the single scattering contribution from the multiple scattering contribution. The multiple scattering contribution is solved in the Fourier space.

The forward model relies on the same atmospheric vertical structure as in Govaerts et al. (2010), *i.e.*, a three-level system containing two layers that are radiatively coupled (Figure 1). The height of level Z_a is determined from an aerosol height climatology derived from level 3 aerosol profile product obtained with the CALIOP (Cloud- Aerosol LIdar with Orthogonal Polarization) instrument on-board CALIPSO might be considered. The aerosol profile product reports monthly mean profiles of aerosol optical properties on a uniform global spatial grid. The spatial resolution is 5° in longitude, 2° in latitude and 60 m along vertical. This is a tropospheric product that reports averaged values at altitudes below 12km. The lower level z_0 is the surface. Over land surface reflectance is represented by the so-called RPV model which has four parameters (ρ_0, k, Θ, h) that are all wavelength dependent (Rahman et al. 1993). Over sea surface, BRF is simulated with the Cox-Munk model as implemented in Vermote et al. (1997). The lower layer L_a, ranging from level z_p to z_a contains the aerosol particles. Molecular scattering and absorption are also taking place in that layer. The upper layer L_g, ranging from z_a to z_s is only subject to molecular absorption. The uncertainty of this model is estimated on Section 4.2.4.3.

3.2 General mathematical formulation

The FASTRE model expresses the TOA BRF in a given spectral band $\tilde{\lambda}$ as a sum of the single $I_s^{\uparrow}$ and multiple $I_m^{\uparrow}$ scattering contributions as in

$$y_m(\mathbf{x}, \mathbf{b}; \mathbf{m}) \;=\; T_{L_g}(\mathbf{b}; \mathbf{m}) \, \frac{I_s^{\uparrow}(\mathbf{x}, \mathbf{b}; \mathbf{m}) \;+\; I_m^{\uparrow}(\mathbf{x}, \mathbf{b}; \mathbf{m})}{E_0^{\downarrow}(\mathbf{m})\mu_0} \tag{1}$$

where

$I_s^{\uparrow}(\mathbf{x}, \mathbf{b}; \mathbf{m})$ is the upward radiance field at level Z_a due to the single scattering;

$I_m^{\uparrow}(\mathbf{x}, \mathbf{b}; \mathbf{m})$ is the upward radiance field at level Z_a due to the multiple scattering;

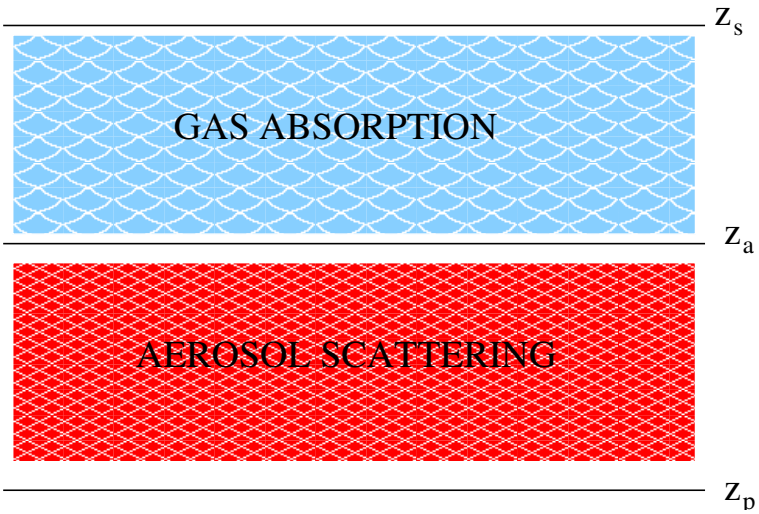

Figure 1: FASTRE forward model vertical structure. z_p is the pixel elevation, z_a the height of the aerosol layer above z_p and z_s the top of the gas absorption layer.

$T_{L_g}(\mathbf{b};\mathbf{m})$ denotes the total transmission factor in the L_g layer;

$E_0^{\downarrow}(\mathbf{m})$ denotes the solar irradiance at level Z_s corrected for the Sun-Earth distance variations.

The single scattering contribution writes

$$I_s^{\uparrow}(\mathbf{x},\mathbf{b};\mathbf{m}) = \frac{E_0^{\downarrow}(\mathbf{m})\ \mu_0}{\pi} \exp\left(\frac{-\tau_{L_a}}{\mu_0}\right)\ r_s(\mathbf{x_s},\mathbf{b};\mathbf{m})\ \exp\left(\frac{-\tau_{L_a}}{\mu_v}\right) \tag{2}$$

where τ_{L_a} is the total optical thickness of layer L_a. μ_0 and μ_v are the cosine of the illumination and viewing zenith angles respectively.

The multiple scattering contribution $I_m^{\uparrow}(\mathbf{x},\mathbf{b};\mathbf{m})$ is solved in the Fourier space in all illumination and viewing directions of the quadrature directions N_θ for $2N_\theta - 1$ azimuthal directions. The contribution $I_m^{\uparrow}(\mathbf{x},\mathbf{b};\mathbf{m})$ in the direction (Ω_0,Ω_v) is interpolated from the surrounding quadrature directions.

3.3 Surface properties

3.3.1 Land surface

The surface reflectance at z_p is represented by the RPV model (Rahman et al. 1993) which has four parameters $\mathbf{x}_s = (\rho_0, k, \Theta, h)$ that are all wavelength dependent. The individual contribution of these four parameters to the total surface BRF is illustrated on Figure (2). Specifically,

ρ_0 controls the mean amplitude of the BRF. This parameter strongly varies with the wavelength and mainly controls the mean surface reflectance. It varies between 0 and 1.

k determines the bowl shape of the BRF. It varies between 0 and 2.

Θ is the asymmetry parameter of the Henyey-Greenstein phase function and also varies between -1 and 1.

h controls the amplitude of the hot-spot, *i.e.*, the "porosity" of the medium. This parameter takes only positive values and typically varies between 0 and 1.

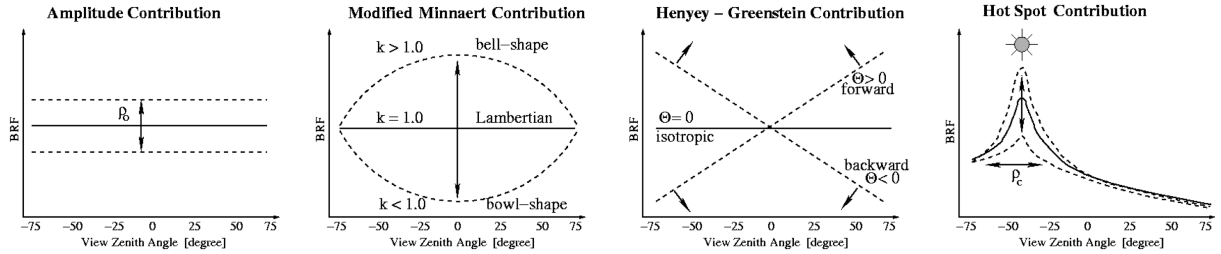

Figure 2: Contribution of the four RPV parameters to the total surface BRF.

Engelsen et al. (1996) analysed in detail on the performance and limits of applicability of this parametric model. The RPV model formally writes

$$r_s(\mathbf{x}, \mathbf{b}; \mathbf{m}) = \rho_0(\tilde{\lambda})\, \breve{\rho}_s(k(\tilde{\lambda}), \Theta(\tilde{\lambda}), h(\tilde{\lambda}); \mu_0, -\mu_v, \phi_r) \tag{3}$$

where ρ_0 and $\breve{\rho}_s(k(\tilde{\lambda}), \Theta(\tilde{\lambda}), h(\tilde{\lambda}); -\mu_v, \mu_0, \phi_r)$ describe the amplitude and the angular field of the surface BRF, respectively. This latter quantity is expressed by:

$$\breve{\rho}_s(k(\tilde{\lambda}), \Theta(\tilde{\lambda}), h(\tilde{\lambda}); \mu_0, -\mu_v, \phi_r) = M_I(\mu_0, -\mu; k(\tilde{\lambda}))\, F(g; \Theta(\tilde{\lambda}))\, H(h(\tilde{\lambda}); G) \tag{4}$$

where:

$$M_I(\mu_0, -\mu; k(\tilde{\lambda})) = \frac{\mu_0^{k-1}\mu^{k-1}}{(\mu_0 + \mu_v)^{1-k}} \tag{5}$$

$$F(g; \Theta(\tilde{\lambda})) = \frac{1 - \Theta^2(\tilde{\lambda})}{[1 + 2\Theta(\tilde{\lambda})\cos g + \Theta^2(\tilde{\lambda})]^{3/2}} \tag{6}$$

$$H(h(\tilde{\lambda}); G) = 1 + \frac{1 - h(\tilde{\lambda})}{1 + G} \tag{7}$$

$$\cos g = \cos\theta \cos\theta_0 + \sin\theta \sin\theta_0 \cos\phi_r \tag{8}$$

$$G = [\tan^2\theta_0 + \tan^2\theta - 2\tan\theta_0 \tan\theta \cos\phi_r]^{1/2} \tag{9}$$

The relative azimuth angle, ϕ_r, is zero when the source of illumination is behind the satellite.

3.3.2 Sea surface

The total reflectance over sea surfaces is defined as being composed of three terms, representing three different sources of upwelling radiance fields. Firstly, light can be reflected off white caps in the rough ocean surface; secondly, it can be reflected off the sea surface itself. The relative contributions from these two factors will depend on the roughness of the sea surface, which is dependent on the surface

wind speed v_{z_0}. Thirdly, light penetrating the surface can be scattered back up into the atmosphere by molecules within the water, such as water and dissolved pigments. Considering the combination of these terms, the sea surface reflectance in spectral band $\tilde{\lambda}$ writes

$$r_s(\mathbf{x}, \mathbf{b}; \mathbf{m}) = \rho_{wc}(v_{z_0}; \tilde{\lambda}) + (1 - W)\rho_{gl}(v_{z_0}; \tilde{\lambda}) + (1 - \rho_{gl}(v_{z_0}; \tilde{\lambda}))\rho_{sw} \tag{10}$$

where

ρ_{wc} is the reflectance due to white caps

ρ_{gl} is the specular reflectance at the ocean surface

ρ_{sw} is the scattered reflectance emerging from sea water

W is the relative area covered with white caps

v_{z_0} is the surface wind speed.

The reflectance of the white cap is taken from Koepke (1984) and the specular contribution from Cox and Munk (1954). For the scattered reflectance emerging from sea water, a constant chlorophyll concentration of 0.1 [mg/m^3] is assumed (Morel 1988).

3.4 Scattering layer properties

The layer L_a contains a set of mono-mode aerosol classes v characterized by their single scattering properties, *i.e.*, the single scattering albedo $\omega_{0,v}(\tilde{\lambda})$ and phase function $\Phi_v(\tilde{\lambda}, \Omega_g)$ in the spectral bands $\tilde{\lambda}$ at the phase angle Ω_g. These classes define the vertices encompassing the solution space. The different vertices representing fine and coarse mode aerosols are combined into this layer according to their respective optical thickness $\tau_v(\tilde{\lambda})$ with the total aerosol optical thickness $\tau_a(\tilde{\lambda})$ of the layer being equal to

$$\tau_a(\tilde{\lambda}) = \sum_v \tau_v(\tilde{\lambda}) \tag{11}$$

The phase function $\Phi_v(\tilde{\lambda}, \Omega_g)$ of an aerosol vertex is characterized by a limited number N_κ of Legendre coefficients equal to $2N_\theta - 1$ where N_θ is the number of quadrature points used to solve the multiple scattering integral. The choice of this number results from a trade-off between accuracy and computer time. When N_κ is too small, the last Legendre moment is often not equal to zero and the delta-M approximation is applied (Wiscombe 1977). In that case, the α_d coefficient of the delta-M approximation is equal to $\Phi_v(N_\kappa)$. The Legendre coefficients κ_j, after application of the delta-M approximation, become

$$c_j = \frac{\kappa_j - \alpha_d}{1 - \alpha_d} \tag{12}$$

and the truncated phase function denoted Φ'_v. The corrected optical thickness $\tau'_v(\tilde{\lambda})$ and single scattering albedo $\omega'_{0,v}(\tilde{\lambda})$ of the corresponding aerosol class become

$$\tau'_v(\tilde{\lambda}) = (1 - \omega_{0,v}\alpha_d)\,\tau_v(\tilde{\lambda}) \tag{13}$$

and

$$\omega'_{0,v}(\tilde{\lambda}) = \frac{1-\alpha_d}{1-\omega_{0,v}\alpha_d}\,\omega_{0,v}(\tilde{\lambda})\ . \tag{14}$$

The layer total optical thickness, τ_{L_a}, is the sum of the gaseous, τ_g, the aerosol, τ'_a and the Rayleigh, τ_r, optical depth

$$\tau_{L_a}(\tilde{\lambda}) = \tau_g(\tilde{\lambda}) + \tau'_a(\tilde{\lambda}) + \tau_r(\tilde{\lambda}) \tag{15}$$

with $\tau'_a(\tilde{\lambda}) = \sum_v \tau'_v(\tilde{\lambda})$. The single scattering albedo of the scattering layer is equal to

$$\omega'_0(\tilde{\lambda}) = \frac{\sum_c \omega'_{0,v}(\tilde{\lambda})\ \tau'_v(\tilde{\lambda})}{\tau'_a(\tilde{\lambda})} \tag{16}$$

and the layer average phase function

$$\Phi'(\tilde{\lambda}, \Omega_g) = \frac{\sum_c \Phi'_v(\tilde{\lambda}, \Omega_g)\ \tau'_v(\tilde{\lambda})}{\tau'_a(\tilde{\lambda})}\ . \tag{17}$$

3.5 Gaseous layer properties

It is assumed that only molecular absorption is taking place in the gaseous layer. The height of level z_a is used to partition the TCWV and TCO3 concentration in each layer assuming a US76 standard atmosphere vertical profile. T_{L_g} denotes the total transmission of that layer.

3.6 Forward model gradients

The derivatives $\mathbf{K}_x$ (Jacobian matrix) with respect to the forward model $y_m(\mathbf{x}, \mathbf{b}; \mathbf{m})$ are calculated as forward finite differences.

3.7 State vector

The state vector $\mathbf{x}$ is composed of the parameters $\mathbf{x}_s$ defining the surface reflectance $r_s(\mathbf{x}, \mathbf{b}; \mathbf{m})$ in the four PROBA-V bands and the aerosol fine and coarse mode optical thickness $\mathbf{x}_a = \{\tau_f, \tau_c\}$.

The state parameters defining the radiative properties of the observed medium are divided into two categories. The first one, noted $\mathbf{x}$, represents the state variables that are retrieved from the observations $\mathbf{y}_{\Omega\tilde{\Lambda}}$ and is referred to as the *state vector*. The second one, noted $\mathbf{b}$, represents those parameters that also have a non-negligeable radiative effects on the observed medium but may not be reliably estimated from those measurements. They are referred to as the *model parameters* and are obtained from external source of information. The size of the state vector is noted n_x.

The model parameters are composed of the ozone U_{O_3}, water vapour total column content U_{H_2O}, surface pressure P_{z_0}, surface wind speed v_{z_0} and direction v_ϕ, and aerosol layer height z_a.

$$\mathbf{b} = \left\{U_{O_3}, U_{H_2O}, P_{z_0}, v_{z_0}, v_\phi, z_a\right\}. \tag{18}$$

Surface pressure is derived from the Global Land Surface Digital Elevation Model (GLSDEM). Water vapour is taken from Numerical Weather Prediction (NWP) model data deliverd by MeteoServices. Ozone total column content is retrieved from a climatology based on Total Ozono Mapping Spectrometer (TOMS) observations prepared by the Centre dÉtude Spatiales de la Biosphére (CESBIO). Surface wind speed and direction are taken from European Centre for Mid-Range Weather Forecasts (ECMWF) data. The aerosol layer height z_a is set to 2km. The surface wind speed is used only over water.

4 ALGORITHM DESCRIPTION

4.1 Outline

The CISAR algorithm is composed of the following major steps:

1. **Pre-processing**
   A series of pre-processing operations are performed prior to the inversion. The primary purpose of this pre-processing is the accumulation of PROBA-V data during a given period to form a multi-spectral and multi-angular observation vector. It also collects ancillary information required for the inversion and perform some additional computations such as observation uncertainty estimation and prior information definition. These pre-processing steps are:

   (a) Input data accumulation (Section 4.2)
   In this step, all information needed to perform the inversion is collected and accumulated. It concerns essentially the preparation of the measurement vector. For each pixel, PROBA-V radiances are accumulated during several days together with requested ancillary information such as the cloud mask, the total gaseous amount, the geometry, band irradiance and finally all relevant information for the computation of the radiometric uncertainties.

   (b) *a priori* information definition (Section 4.2.3)
   The *a priori* information is prepared from the best retrieval selected in the temporal compositing of the previous application cycle or default values when the processing of a time series is initiated.

   (c) Measurement noise estimation (Section 4.2.4)
   The radiometric noise of the observation vector is estimated.

2. **Angular and Spectral Inversion**
   The angular and spectral inversion for the retrieval of the aerosol and surface reflectance properties is performed individually for every processed pixel.

   (a) Cloud filtering (Section 4.3.1)
   A cloud mask is applied on the observation vector to remove all the cloud observations.

   (b) Inversion (Section 4.3.2.1)
   The state vector is estimated from the measurement vector. The forward model is estimated at each inversion step.

   (c) Retrieval uncertainty estimation (Section 4.3.4)
   The uncertainty of the solution is estimated.

   (d) Quality control (Section 4.3.3)
   A quality indicator based on factors such as the magnitude of the Jacobians of the AOT and the residual of the cost function is calculated.

3. **Product generation** (Section 4.4)

   The CISAR algorithm delivers the surface BHR and RPV parameters in each processed spectral band, as well as the AOT at 0.55μm.

4.2 Pre-processing

This module collects all the information needed to perform the inversion. These data are listed in Section (6).

4.2.1 PROBA-V observations

The observation information consists of all available daylight clear-sky slots acquired under different illumination conditions in the 0.4, 0.6, 0.8 and 1.6μm PROBA-V bands. These observations are accumulated during a period of N_d days to form a multi-angular observation vector. PROBA-V acquires radiances $R(\Omega_0, \Omega_v, \tilde{\lambda}, z_s, \mathbf{p})$ with the geometry $\Omega = (\Omega_0, \Omega_v)$ in a spectral interval $\tilde{\lambda}$ when the radiometer is viewing a pixel $\mathbf{p}$ on the Earth from the level z_s. Only observations acquired with sun and viewing zenith angles smaller than $\theta_{\max}$ are considered.

The accumulation period is characterized by a time length of N_d days which is shifted by N_s days, as shown in Figure 3. This allows a good trade-off between the need to accumulated enough cloud-free and multi-angular observations and possible variations of the surface, which is assumed temporally invariant during the accumulation period. This features is particular important when few observations per accumulation period are available which require to increase the length of the accumulation period.

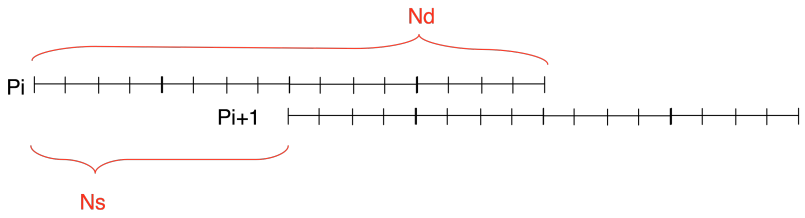

Figure 3: Definition of accumulation periods of N_d days which is shifted by N_s days.

For the purpose of the retrieval process, these radiances are converted into BRF with

$$\mathbf{y}(\Omega_0, \Omega_v, \tilde{\lambda}, \mathbf{p}) = \mathbf{y}(t, \tilde{\lambda}, \mathbf{p}) = \frac{\pi\, R(\Omega_0, \Omega_v, \tilde{\lambda}, z_s, \mathbf{p})\, d_{\odot}^2(t)}{E_0(\tilde{\lambda}, z_s)\, \mu_0} \tag{19}$$

where $d_{\odot}$ is the Sun-Earth distance at time t in Astronomical Unit (AU) and $E_0(\tilde{\lambda})$ is exo-atmospheric solar irradiance in the PROBA-V channel $\tilde{\lambda}$. $\{\Omega_0, \Omega_v, \tilde{\lambda}, z_s, \mathbf{p}\}$ constitute the independent parameters determining the observation conditions and are denoted $\mathbf{m} = \{\Omega_0, \Omega_v, \tilde{\lambda}, z_s, \mathbf{p}\}$.

For a given band, all observations sequentially accumulated during N_d days to form a virtual multi-angular observation system. The corresponding measurement vector is noted

$$\mathbf{y}_{\Omega}(\tilde{\lambda}, z_s, \mathbf{p}) = \mathbf{y}_m(\Omega_0(t_1), \cdots, \Omega_0(t_N), \Omega_v, \tilde{\lambda}, z_s, \mathbf{p}) = \mathbf{y}_m(t_1, \cdots, t_N, \Omega_v, \tilde{\lambda}, z_s, \mathbf{p}) = \mathbf{y}_{\Omega\tilde{\lambda}}(\Omega_v, z_s, \mathbf{p}). \tag{20}$$

When all spectral bands are considered, the measurement vector is noted in one of the following two way

$$\mathbf{y}_{\Omega\tilde{\Lambda}} = \{\mathbf{y}_\Omega(\tilde{\lambda}_1), \mathbf{y}_\Omega(\tilde{\lambda}_2), \mathbf{y}_\Omega(\tilde{\lambda}_3)\} \quad (21)$$

$$\mathbf{y}_{T\tilde{\Lambda}} = \{\mathbf{y}_T(\tilde{\lambda}_1), \mathbf{y}_T(\tilde{\lambda}_2), \mathbf{y}_T(\tilde{\lambda}_3)\} \quad (22)$$

4.2.2 Model parameters

The model parameters $\mathbf{b} = \left\{U_{O_3}, U_{H_2O}, P_{z_0}, v_{z_0}, v_\phi, z_a\right\}$ are first interpolated into the satellite projection. The following fields undergo additional processing:

U_{H_2O} TCWV is provided at the sea level z_0. The actual TCWV is rescaled at the actual pixel elevation z_p as follows:

(a) The elevation of the geopotential is retrieved from interpolated ECWMF data.

(b) Calculate the TCWV using the FASTRE standard vertical profile and geopotential height

(c) Determine a rescaled profile using the retrieved TCWV and the calculated TCWV.

(d) Use the rescaled profile and the actual pixel elevation to determine the actual TCWV.

P_{z_0} The surface pressure given by the ECWMF data provided at the sea level z_0 is calculated at the actual pixel elevation z_p with

$$P_{z_p} = P_{z_0} * \exp\left(\frac{g\,M\,(z_0 - z_p)}{R_0\,T_{z_0}}\right), \quad (23)$$

g being the Earth-surface gravitational acceleration, M the molar mass of dry air, R_0 the universal gas constant and T_{z_0} the sea level standard temperature.

z_a The aerosol layer height z_a is retrieved from the climatological data set generated by Kinne et al. (2013). This data set provide the vertical profile of extinction coefficient. The aerosol layer height is defined as the elevation corresponding to 80% of the vertical integrated extinction coefficient.

4.2.3 Prior information

4.2.3.1 Prior information on the surface parameter magnitude The prior information $\mathbf{x}_b$ on the state of the surface $\mathbf{x}_s$ is defined from the analysis of the solutions $\hat{\mathbf{x}}(d)$ retrieved during the processing of the previous accumulation period. When CISAR runs for the first time, the prior information $\mathbf{x}_b$ of $\mathbf{x}_s$ is a default or climatological values with a corresponding very large uncertainties σ_{x_b}.

After the processing of the first accumulation period, prior information $\mathbf{x}_b$ is updated with the *a posteriori* solution. Specifically, the running mean and range in which the parameters vary are estimated based on the previous solutions during a certain time window N_r days long. Hence, the at prior information $\mathbf{x}_b$ time t_d the estimation of the prior information $\mathbf{x}_b(t_d)$ and associated uncertainty $\sigma_{x_b}(t_d)$ write

$$\mathbf{x}_b(t_d) = \frac{\sum_{t_i=0}^{t_d-1} \hat{\mathbf{x}}(t_i)}{N_r} \quad (24)$$

$$\sigma_{x_b}(t_d) = \frac{\max_{t_i \in N_r} \hat{\mathbf{x}}(t_i) - \min_{t_i \in N_r} \hat{\mathbf{x}}(t_i)}{2} \quad (25)$$

When not enough solutions $\hat{\mathbf{x}}(t_i)$ are available in the interval N_r, the prior information of the accumulation period t_d and its associated uncertainty are taken from the results of the previous accumulation period index $t_d - 1$. Such situation will typically occur at the beginning of a processing. If the processing of the last period $t_d - 1$ is successful, the surface prior value at t_d is updated to

$$\mathbf{x}_b(t_d) = \hat{\mathbf{x}}(t_d - 1) \quad (26)$$

$$\sigma_{x_b}(t_d) = \max(\sigma_{\hat{\mathbf{x}}}(t_d - 1), \sigma_{\min}) \quad (27)$$

where $\sigma_{\min}$ is the smallest allowed uncertainty on the surface prior values. Additionally, the update of $\mathbf{x}_b(t_d)$ is constrained by the following conditions

$$\left(\frac{\mathbf{x}_b(t_d)}{t_d}\right)^2 < (\sigma_{\min})^2 \quad (28)$$

When the processing of the previous period is not successful, *e.g.*, there were too few observations, the prior is kept with the same value, *i.e.*, $\mathbf{x}_b(t_d) = \mathbf{x}_b(t_d - 1)$ and the associated uncertainty is set to

$$\sigma_{x_b}(t_d) = \sigma_{x_b}(t_d - 1)\ 1.05^{N_d} \quad (29)$$

such that if this situation lasts several accumulation periods, the uncertainty of $\mathbf{x}_b$ will become larger and larger. The values σ_{x_b} are stored in the $\mathbf{S}_x$ matrix.

4.2.3.2 Prior information on the aerosol optical thickness

The prior information on the magnitude of AOT is set to very low value with a large corresponding uncertainty. When there is an overlap between two consecutive accumulation periods, the retrieved AOT of the first period is used as prior information for the second period in the overlapping time frame.

4.2.3.3 Prior information on the surface parameter spectral variability

Prior information concerning the spectral dependency of the surface anisotropy could also be used. The spectral variations of the surface anisotropy k, Θ and h are expected to be subject to some spectral dependencies. In the MISR aerosol algorithm for instance, this correlation is expressed as a spectral invariance of the normalized shape of the BRF (Diner et al. 2005). Spectral similarities in the surface reflectance are used to determine the correlation $r_{\tilde{\lambda}_i,\tilde{\lambda}_j}(x_s, \Omega)$ of each parameter x_s between bands $\tilde{\lambda}_i$ and $\tilde{\lambda}_j$. The elements of $\mathbf{S}_x$ write

$$\mathbf{S}_x(i,j) = r_{\tilde{\lambda}_i,\tilde{\lambda}_j}(x, \Omega)\, \sigma_i\, \sigma_j. \quad (30)$$

4.2.3.4 Prior information on AOT temporal variability AOT is not expected to change rapidly on an hourly basis. Hence, the speed at which AOT can change in time is constrained. In order to derive the equation of this error contribution, let us define the stochastic variable x as being the deviation between the state variable and its mean such that

$$x = X - \overline{X} \tag{31}$$

The variable x is assumed to be a white noise process, so that $E\{x\} = 0$ and $E\{x^2\} = \sigma_x^2$. Assuming that the daily aerosol load variations are represented by a first order auto regressive model, the equation that describes in time the evolution of x can be written

$$x_{t+1} = \alpha\, x_t + \beta \tag{32}$$

where α is the autocorrelation coefficient between time t and $t+1$, derived from AERONET data temporal analysis, and β is a white noise process.

If x_{t_i} is the value of the state variable at time t_i, it is possible to derive the value of x_{t_j} at time t_j by applying recursively Equation (32). It can be easily shown that an expression of an estimate of the difference between x_{t_j} and x_{t_i} can be written as

$$x_{t_j} - x_{t_i} = \left(\alpha^j - 1\right)\; x_{t_i} + \alpha^{j-1} \cdot \beta_1 + \ldots + \beta_j \tag{33}$$

The uncertainty associated to the assumption $x_{t_j} - x_{t_i} = 0$ is defined as

$$\sigma_A^2(t_{i,j}, \tilde{\lambda}) = \left(A_d + \frac{A_a}{1 + \exp(-A_b\,(|t_i - t_j| - A_c))} \right)^2 \tag{34}$$

The values of the coefficients A_a, A_b, A_c and A_d are given in Section (6.1). The elements of $\sigma_A^2(t_{i,j})$ are stored in the $\mathbf{S}_a$ matrix. The resulting model is shown in Figure 4.

Figure 4: AOT temporal smoothness model.

4.2.3.5 Prior information on AOT spectral variability Similarly, constraints on the spectral variability of the AOT can be used as suggested by Dubovik et al. (2011). This dependency is used to determine the correlation of $\tau_a(\tilde{\lambda})$ between bands $\tilde{\lambda}_i$ and $\tilde{\lambda}_j$. Within a pre-defined aerosol class c, we have

$$\tau_c(\tilde{\lambda}_i) = \tau_c(\tilde{\lambda}_j)\ \frac{\sigma_e(\tilde{\lambda}_i)}{\sigma_e(\tilde{\lambda}_j)} \tag{35}$$

where σ_e is the extinction coefficient. As each optical thickness in each processed spectral band $\tilde{\lambda}$ for a given aerosol class is retrieved independently, the spectral variation of τ_c is constrained assuming that the retrieved optical thickness $\tau_c(\tilde{\lambda}_i)$ in band $\tilde{\lambda}_i$ could be related to the one in band $\tilde{\lambda}_j$ with Equation (35) assuming a constant error σ_L.

4.2.4 Measurement system uncertainty

A reliable estimation of the measurement system uncertainty is one of the most critical aspects of the CISAR algorithm as it strongly determines the likelihood of the solution. The measurement system total error covariance matrix $\mathbf{S}_y$ is composed of

$$\mathbf{S}_y = \mathbf{S}_N + \mathbf{S}_B + \mathbf{S}_F \tag{36}$$

with

S_N the radiometric noise matrix;

S_B the equivalent model parameter matrix;

S_F the forward model uncertainty matrix.

All uncertainties are expressed in BRF. The elements i, j of $\mathbf{S}_y$ are composed of

$$\mathbf{S}_y(i,j) = \begin{pmatrix} \sigma^2(\bar{t}_0,\tilde{\lambda}_1) & r_{12}\sigma(\bar{t}_0,\tilde{\lambda}_1)\sigma(\bar{t}_1,\tilde{\lambda}_1) & \cdots & r_{1N}\sigma(\bar{t}_0,\tilde{\lambda}_1)\sigma(\bar{t}_N,\tilde{\lambda}_1) & r_{1N+1}\sigma(\bar{t}_0,\tilde{\lambda}_1)\sigma(\bar{t}_1,\tilde{\lambda}_2) & \cdots & r_{1M_y}\sigma(\bar{t}_0,\tilde{\lambda}_1)\sigma(\bar{t}_N,\tilde{\lambda}_3) \\ r_{21}\sigma(\bar{t}_1,\tilde{\lambda}_1)\sigma(\bar{t}_0,\tilde{\lambda}_1) & \sigma^2(\bar{t}_1,\tilde{\lambda}_1) & \cdots & \cdots & \cdots & \cdots & r_{2M_y}\sigma(\bar{t}_1,\tilde{\lambda}_1)\sigma(\bar{t}_N,\tilde{\lambda}_3) \\ \vdots & \cdots & \ddots & \cdots & \cdots & \cdots & \vdots \\ r_{2M_y}\sigma(\bar{t}_0,\tilde{\lambda}_1)\sigma(\bar{t}_N,\tilde{\lambda}_3) & \cdots & \cdots & \cdots & \cdots & \ddots & \sigma^2(\bar{t}_N,\tilde{\lambda}_3) \end{pmatrix} \tag{37}$$

4.2.4.1 Radiometric uncertainty $\mathbf{S}_N$ Within CISAR, the difference in the spectral spectral response of each Proba-V camera is not accounted for but is considered as part of the measurement uncertainty, assuming the same mean spectral response function for each camera. Similarly, the viewing angles difference of the SWIR camera is not accounted for. These assumptions are converted into equivalent radiometric uncertainties.

The total radiometric uncertainty is thus composed of

σ_i the instrument radiometric noise;

σ_c the difference between the spectral response of the three Proba-V cameras;

σ_θ the difference between the viewing angles in the SWIR band and the viewing angles in the other bands;

σ_r the geo-location/coregistration accuracy.

The contribution σ_i is dependent on the camera and the band. It is expressed as a percentage of the measurement vector $\mathbf{y}_{\Omega\tilde{\Lambda}}$ and it assumes the following values:

Band	Camera	Radiometric uncertainty
BLUE	All	4%
RED	All	3%
NIR	All	3%
SWIR	Center	4%
SWIR	Left, Right	5%

The contribution σ_c is due to the difference between the spectral response of the three cameras and the mean spectral response used in the algorithm (Figure 5). It writes:

$$\sigma_c^2(\tilde{\lambda}) = \frac{\left(\frac{\int y(\tilde{\lambda})\xi_M(\tilde{\lambda})d\tilde{\lambda}}{\int \xi_M(\tilde{\lambda})d\tilde{\lambda}} - \frac{\int y(\tilde{\lambda})\xi_{L/C/R}(\tilde{\lambda})d\tilde{\lambda}}{\int \xi_{L/C/R}(\tilde{\lambda})d\tilde{\lambda}}\right)}{\frac{\int y(\tilde{\lambda})\xi_{L/C/R}(\tilde{\lambda})d\tilde{\lambda}}{\int \xi_{L/C/R}(\tilde{\lambda})d\tilde{\lambda}}} \tag{38}$$

This error has been estimated for a large number of different geometries, atmospheric conditions and surface status. The corresponding relative error is about 0.1% in each spectral band. The term $\sigma_c^2(\tilde{\lambda})$ is therefore set equal to $0.001\ \mathbf{y}_{\Omega\tilde{\Lambda}}$.

The contribution σ_θ is present only in the SWIR band and it writes

$$\sigma_\theta^2(\tilde{\lambda},\theta) = \left(\frac{\partial \mathbf{y}(\tilde{\lambda},\theta)}{\partial\theta}\right)^2 \sigma_\theta^2 \tag{39}$$

where σ_θ^2 is the difference between the viewing zenith angle in the SWIR band and the one in the other bands, used in the inversion.

The geo-location/coregistration inaccuracies σ_r needs to be estimated for each pixel of an image

$$\sigma_r^2(t,\tilde{\lambda},\mathbf{p}) = \left(\frac{\partial \mathbf{y}(t,\tilde{\lambda},p_x,p_y)}{\partial p_x}\sigma_x(\bar{t},\tilde{\lambda})\right)^2 + \left(\frac{\partial \mathbf{y}(t,\tilde{\lambda},p_x,p_y)}{\partial p_y}\sigma_y(\bar{t},\tilde{\lambda})\right)^2 \tag{40}$$

where $\sigma_{x,y}$ is the geo-location/coregistration standard deviation of channel $\tilde{\lambda}$ acquired at time $\bar{t}$. It is expected that the rectification noise is spectrally correlated but not temporally correlated. Hence the terms of the matrix $\mathbf{S}_N$ writes

$$\mathbf{S}_N(i,j) = \delta(i,j)\sigma_i^2(\tilde{\lambda}) + \delta(i,j)\sigma_c^2(\tilde{\lambda}) + \delta(i,j)\sigma_\theta^2(\tilde{\lambda},\theta) + r_r(i,j)\sigma_r(i)\sigma_r(j) \tag{41}$$

where $\delta(i,j)$ is the Dirac function ($\delta(i,j) = 0$ when $i \neq j$). The rectification correlation r_r is 1 when i and j concern the same PROBA-V band and 0 otherwise.

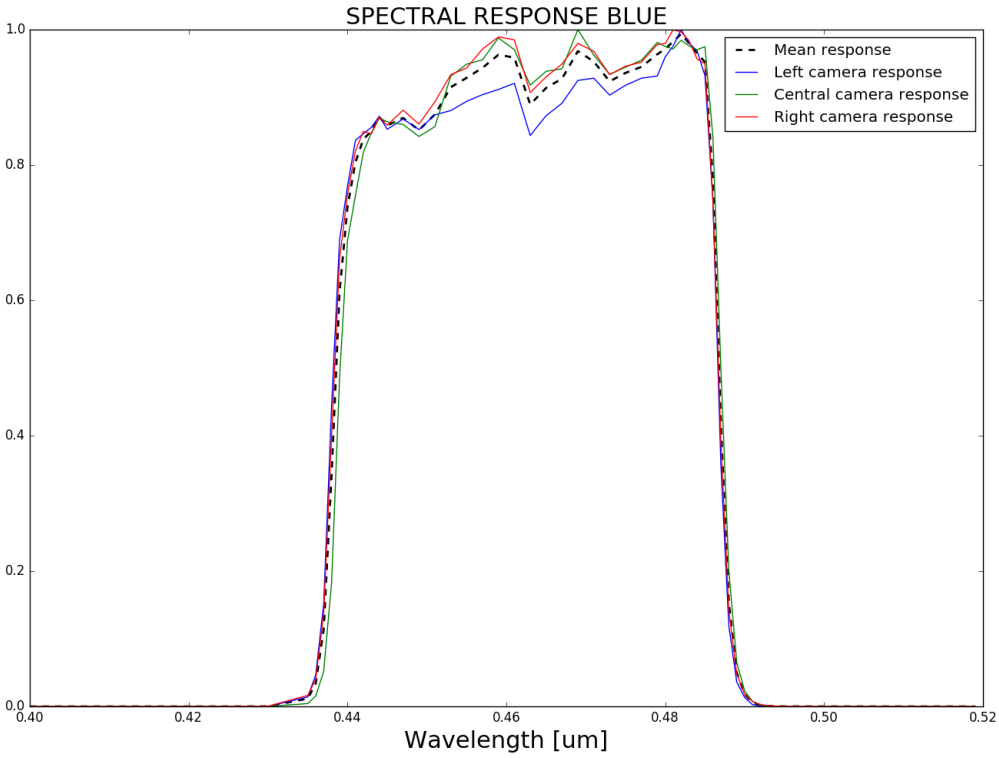

Figure 5: Comparison between the spectral response of the three Proba-V cameras and the mean spectral response.

4.2.4.2 Equivalent model parameter noise $\mathbf{S}_B$ This noise is due to the uncertainties on $\mathbf{b}(\bar{t})$. It is converted in Equivalent Model Parameter Noise (EQMPN). As this piece of information comes from two independent sources of information, they are supposed not correlated.

$$\sigma_B^2(\mathbf{b};\tilde{\lambda},\Omega_0,\Omega_v) = \left(\frac{\partial y(\mathbf{x},U_{oz};\Omega,\tilde{\lambda})}{\partial U_{oz}}\sigma_{U_{oz}}\right)^2 + \left(\frac{\partial y(\mathbf{x},U_{wv};\Omega,\tilde{\lambda})}{\partial U_{wv}}\sigma_{U_{wv}}\right)^2 \tag{42}$$

The terms of the matrix $\mathbf{S}_B$ write

$$\mathbf{S}_B(i,j) = \delta(i,j)\,\sigma_B^2(\tilde{\lambda},\Omega) \tag{43}$$

4.2.4.3 Forward model uncertainty $\mathbf{S}_F$ This noise results from fast forward model assumptions and approximations described in Section 3.1. Let $y_R(\mathbf{x},\mathbf{b})$ be an accurate forward model with an explicit representation of the atmospheric vertical profile. A global estimation of this error is performed that does not depend on the actual value of $\mathbf{x}$. The error covariance is

$$\sigma_F^2(\tilde{\lambda},\Omega_0,\Omega_v,\phi) = \Big(\mathbf{y}(\Omega,\tilde{\lambda})\Big)^2 \;\frac{1}{N}\sum_{\{\mathbf{x},\mathbf{b}\}}\left(\frac{y_m(\mathbf{x}_\Delta,\mathbf{b}_\Delta,\Omega_\Delta) - y_R(\mathbf{x},\mathbf{b},\Omega)}{y_R(\mathbf{x},\mathbf{b},\Omega)}\right)^2 \tag{44}$$

where $\mathbf{x}_\Delta$ represents the discretized value of $\mathbf{x}$ and $\{\mathbf{x}, \mathbf{b}\}$ is the domain of variation of $\mathbf{x}$ and $\mathbf{b}$. The terms of the matrix $\mathbf{S}_F$ writes

$$\mathbf{S}_F(i,j) = \sigma_F^2(\tilde{\lambda}, \Omega_0, \Omega_v, \phi) \tag{45}$$

4.3 Angular and spectral inversion

4.3.1 Cloud filtering

The standard PROBA-V cloud mask is used to disregard pixels which are not cloud free. This mask takes the following values:

0 Clear sky
1 Shadow
2 Undefined
3 Cloud
4 Ice

Only clear sky pixels are considered in CISAR.

The size of the measurement vector after cloud screening and data reduction is noted n_y. The inversion process takes place only when the number of clear-sky observations within the accumulation period is larger than $4 + N_a$ where N_a is the number of inverted aerosol classes.

4.3.2 Definition of the cost function J

The fundamental principle of optimal estimation is to maximise the probability of the retrieved state conditional on the value of the measurements and any prior information. Formally, it is required to maximise the conditional probability $P = P(\mathbf{x}|\mathbf{y}_{\Omega\tilde{\Lambda}}, \mathbf{x_b}, \mathbf{b})$ with respect to the values of the state vector $\mathbf{x}$ (Section 3.7), where $\mathbf{x_b}$ is the prior value of the state vector (Section 4.2.3) and $\mathbf{b}$ are all the other elements of the radiative transfer, called forward model parameters (Section 3.7). The assumption is made that uncertainties in the measurements ($\mathbf{S}_y$ Equation 36), and prior ($\mathbf{S}_x$) are normally distributed with zero mean. Then, the conditional probability takes on the quadratic form (Rodgers 2000) or (Dubovik et al. 2011):

$$\begin{aligned} P(\mathbf{x}) \quad \propto \quad & \exp\left[-\left(y_m(\mathbf{x},\mathbf{b};\mathbf{m}) - \mathbf{y}_{\Omega\tilde{\Lambda}}\right)^T \mathbf{S}_y^{-1} \left(y_m(\mathbf{x},\mathbf{b};\mathbf{m}) - \mathbf{y}_{\Omega\tilde{\Lambda}}\right)\right] \\ & \exp\left[-\left(\mathbf{x} - \mathbf{x}_b\right)^T \mathbf{S}_x^{-1} \left(\mathbf{x} - \mathbf{x}_b\right)\right] \\ & \exp\left[-\mathbf{x}^T \mathbf{H}_a^T \mathbf{S}_a^{-1} \mathbf{H}_a \mathbf{x}\right] \\ & \exp\left[-\mathbf{x}^T \mathbf{H}_l^T \mathbf{S}_l^{-1} \mathbf{H}_l \mathbf{x}\right] \end{aligned} \tag{46}$$

where the first two terms represent weighted deviations from measurements and the prior state parameters, respectively, the third the AOT temporal smoothness constraints and the fourth the AOT spectral

constraint, with respective uncertainty matrices $\mathbf{S}_a$ and $\mathbf{S}_l$. The two matrices $\mathbf{H}_a$ and $\mathbf{H}_l$, representing respectively the temporal and spectral constraints, can be written as block diagonal matrices

$$\mathbf{H} = \begin{pmatrix} \mathbf{H}^{\rho_0} & \mathbf{0} & \mathbf{0} & \mathbf{0} & \mathbf{0} \\ \mathbf{0} & \mathbf{H}^{k} & \mathbf{0} & \mathbf{0} & \mathbf{0} \\ \mathbf{0} & \mathbf{0} & \mathbf{H}^{\theta} & \mathbf{0} & \mathbf{0} \\ \mathbf{0} & \mathbf{0} & \mathbf{0} & \mathbf{H}^{\rho_c} & \mathbf{0} \\ \mathbf{0} & \mathbf{0} & \mathbf{0} & \mathbf{0} & \mathbf{H}^{\tau} \end{pmatrix} \tag{47}$$

where the four blocks $\mathbf{H}^{\rho_0}$, $\mathbf{H}^{k}$, $\mathbf{H}^{\theta}$ and $\mathbf{H}^{\rho_c}$ express the spectral constraints between the surface parameters. Their values are set to zero when these constraints are not active. The submatrix $\mathbf{H}^{\tau}_{a}$ can also be written using blocks $\mathbf{H}^{\tau}_{a;\tilde{\lambda},v}$ along the diagonal. For a given spectral band $\tilde{\lambda}$ and aerosol vertex v, the block $\mathbf{H}^{\tau}_{a;\tilde{\lambda},v}$ is defined as follows

$$\mathbf{H}^{\tau}_{a;\tilde{\lambda},v}\ \boldsymbol{\tau}_{\tilde{\lambda},v} = \begin{pmatrix} 1 & -1 & 0 & \dots & \dots \\ 0 & 1 & -1 & 0 & \dots \\ \dots & \dots & \dots & \dots & \dots \\ \dots & \dots & \dots & 1 & -1 \\ \dots & \dots & \dots & \dots & 0 \end{pmatrix} \begin{pmatrix} \tau_{\tilde{\lambda},v,1} \\ \tau_{\tilde{\lambda},v,2} \\ \vdots \\ \tau_{\tilde{\lambda},v,N_t-1} \\ \tau_{\tilde{\lambda},v,1,N_t} \end{pmatrix} \tag{48}$$

In the same way, the submatrix $\mathbf{H}^{\tau}_{l}$ can be written using blocks $\mathbf{H}^{\tau}_{l;v,t}$. For a given aerosol vertex v and time t, the block $\mathbf{H}^{\tau}_{l;v,t}$ is defined as follows

$$\mathbf{H}^{\tau}_{l;v,t}\ \boldsymbol{\tau}_{v,t} = \begin{pmatrix} 0 & 0 & 0 & \dots & 0 \\ -\frac{\epsilon_2}{\epsilon_1} & 1 & 0 & \dots & 0 \\ 0 & -\frac{\epsilon_3}{\epsilon_2} & 1 & \dots & 0 \\ \dots & \dots & \dots & \ddots & 0 \\ \dots & \dots & \dots & -\frac{\epsilon_{N_\lambda}}{\epsilon_{N_\lambda-1}} & 1 \end{pmatrix} \begin{pmatrix} \tau_{1,v,t} \\ \tau_{2,v,t} \\ \tau_{3,v,t} \\ \vdots \\ \tau_{N_{\tilde{\lambda}},v,t} \end{pmatrix} \tag{49}$$

where the ϵ_l represents the uncertainties associated with the AOT spectral constraints of the individual vertex v bounding the solution space. The spectral variations of τ_v between band $\tilde{\lambda}_l$ and $\tilde{\lambda}_{l+1}$ writes

$$\frac{\tau_{\tilde{\lambda}_l,v}}{\tau_{\tilde{\lambda}_{l+1},v}} = \frac{e_{\tilde{\lambda}_l}}{e_{\tilde{\lambda}_{l+1}}} \tag{50}$$

where $e_{\tilde{\lambda}_l}$ the extinction coefficient in band $\tilde{\lambda}_l$.

Maximising the probability function in Equation (46) is equivalent to minimising the negative logarithm

$$J(\mathbf{x}) = J_y(\mathbf{x}) + J_x(\mathbf{x}) + J_a(\mathbf{x}) + J_l(\mathbf{x}) \tag{51}$$

with

$$J_y(\mathbf{x}) = \left(y_m(\mathbf{x},\mathbf{b},\Omega) - \mathbf{y}_{\Omega\tilde{\Lambda}}\right)\ \mathbf{S}_y^{-1}\ \left(y_m(\mathbf{x},\mathbf{b},\Omega) - \mathbf{y}_{\Omega\tilde{\Lambda}}\right)^T \tag{52}$$

$$J_x(\mathbf{x}) = \left(\mathbf{x} - \mathbf{x}_b\right)\ \mathbf{S}_x^{-1} \left(\mathbf{x} - \mathbf{x}_b\right)^T \tag{53}$$

$$J_a(\mathbf{x}) = \mathbf{x}^T\ \mathbf{H}_a^T\ \mathbf{S}_a^{-1}\ \mathbf{H}_a\ \mathbf{x} \tag{54}$$

$$J_l(\mathbf{x}) = \mathbf{x}^T\ \mathbf{H}_l^T\ \mathbf{S}_l^{-1}\ \mathbf{H}_l\ \mathbf{x} \tag{55}$$

Notice that the cost function J is minimized with respect to the state variable $\mathbf{x}$, so that the derivative of J is independent of the model parameters $\mathbf{b}$ which therefore cannot be part of the solution. The need for angular sampling to document the surface anisotropy leads to an unbalanced size of n_x and n_y with $n_y > n_x$ where n_y and n_x represents the number of observations and state variables respectively. According to Dubovik et al. (2006), these additional observations should improve the retrieval as, from a statistical point of view, repeating the same observation implies that the variance of repeated similar observations should decrease. Accordingly, the magnitude of the elements of the covariance matrix should decrease as $1/\sqrt{n_y}$. Thus, repeating similar observations results in some enhancements of retrieval accuracy which should be proportional to the ratio n_y/n_x. Hence, the cost function which is actually minimized is $J_s(\mathbf{x}) = J_y(\mathbf{x}) + n_y/n_x\ (J_x(\mathbf{x}) + J_a(\mathbf{x}) + J_l(\mathbf{x}))$.

4.3.2.1 Minimization of J This section addresses the problem of the minimization of J, *i.e.*, finding the solution $\hat{\mathbf{x}}$. This is an area where many techniques and methods can be employed and where tuning of the adopted scheme can turn out to be as important as the scheme itself. Essentially any method of finding the minimum is acceptable in a sense, with the caveat that in an operational context it must be robust and fast. The particular characteristics of this problem are that:

- **First and second derivatives of J (with respect to $\mathbf{x}$) are available and continuous** , which implies descent algorithms that makes use of the local gradient are possible and these are generally faster than methods that do not.
- **Multiple minima are unlikely** This condition is however not met in the present case, and the solution is searched for different first guess values (see Section 4.3.2.2)
- **J is likely to be approximately quadratic in the region of the solution, far from quadratic elsewhere.** This characteristics is a result of the reasonably strongly non-linear nature of the forward (radiative transfer) problem. It means that quick convergence from a poor starting position is unlikely.

The cost function $J(\hat{\mathbf{x}})$ is minimized, for example using a steepest descent method, or the Levenberg-Marquardt method (combined steepest-descent method / Gauss-Newton method, as described in Section (4.3.2.3)). This minimization is performed individually for each defined aerosol class.

The first and second derivatives of J with respect to $\mathbf{x}$ are given by:

$$\mathbf{J}' = \frac{\partial J}{\partial \mathbf{x}} = \mathbf{K}_x^T \mathbf{S}_y^{-1}(y_m(\mathbf{x}, \mathbf{b}, \Omega) - \mathbf{y}_{\Omega\tilde{\Lambda}}) + \mathbf{S}_x^{-1}\ (\mathbf{x} - \mathbf{x}_b) + \mathbf{H}_a^T\ \mathbf{S}_a^{-1}\ \mathbf{H}_a\ \mathbf{x} + \mathbf{H}_l^T\ \mathbf{S}_l^{-1}\ \mathbf{H}_l\ \mathbf{x} \quad (56)$$

$$\mathbf{J}'' = \frac{\partial^2 J}{\partial \mathbf{x}^2} = \mathbf{K}_x^T\ \mathbf{S}_y^{-1}\ \mathbf{K}_x + \mathbf{S}_x^{-1} + \mathbf{H}_a^T\ \mathbf{S}_a^{-1}\ \mathbf{H}_a + \mathbf{H}_l^T\ \mathbf{S}_l^{-1}\ \mathbf{H}_l \quad (57)$$

The expression for $\mathbf{J}''$ is a commonly used approximation in that $\mathbf{K}_x$ is assumed to be independent of $\mathbf{x}$, *i.e.*, the radiative transfer is linear in $\mathbf{x}$. The estimation of the Jacobian matrix $\mathbf{K}_x$ is described in Section (3.6). This is only strictly true near the solution (in the region where J is quadratic) but (see next section) since $\mathbf{J}''$ is only employed near the solution the approximation is acceptable.

4.3.2.2 First guess As the problem to be solved is not linear, the presence of local minima is very likely to happen. Hence, when a minimum value is found, an exploration should be made around a minimum in order to determine whether or not it is a local minimum. Such exploration phase could be computationally expensive. This is particularly true when solving a coupled surface-atmosphere system where the magnitude of the surface reflectance is competing with aerosol scattering. It is therefore necessary to carefully select the first guess value $\mathbf{x_0}$ in order to minimize the chance to end in a local minimum.

As the surface parameters $\mathbf{x_s}$ are assumed constant during the accumulation period, only one set of first guess value has to be provided. This value is derived from the prior information $\mathbf{x_b}$

$$\mathbf{x_0}(t_d) = \mathbf{x_b}(t_d) + -1^{t_d}\ \alpha_0\ \sigma_{\mathbf{x_b}}(t_d) \tag{58}$$

where t_d is the index of the processed period and α_0 a perturbation factor.

For the hourly AOT parameter, the first guess values of are set alternatively to a low value τ_{low} and a large one τ_{high}.

4.3.2.3 Marquardt descent algorithm To find the minimum a "first guess" state vector $\mathbf{x}_0$ is selected as described in Section 4.3.2.2 and proceed to make steps, $\delta\mathbf{x}_n$, adjusting the length of the steps according to the distance from the minimum, *i.e.*the lenght of steps decreases when approaching the solution. Assuming the value of J decreases at each step then the updated $\mathbf{x}$ vector is taking the process towards the cost function minimum. The CISAR algorithm relies on the Levenberg-Marquardt method to compute the descent. The use of this algorithm is consistent with the three points made above. The rationale of the Levenberg-Marquardt algorithm is to use a weighted combination of *steepest descent* and *Gauss-Newton descent* according to the characteristics of the cost function. Thus, when the cost function is near quadratic (generally near the solution) the efficiency of the Gauss-Newton algorithm is employed and when the cost function is far from quadratic (generally when far from the solution) the robustness of the Steepest Descent algorithm is favoured.

The Steepest Descent algorithm is intuitively the simplest. The vector $-\mathbf{J}'$ defines the "downward" direction of the local steepest gradient. A move $\delta\mathbf{x} = -\mathbf{J}'$ is almost certainly at least approximately in the direction of the minimum although it may be too far or barely far enough. The step is therefore usually scaled, $\delta\mathbf{x} = -\alpha\mathbf{J}'$ where α is variable. If J is found to be decreasing α can be increased to move faster; if J increases then α is reduced until J decreases. J must eventually decrease with this method otherwise something is wrong with the calculation of $\partial J/\partial\mathbf{x}$. The problem with steepest descent is that it can be very slow to converge, especially near the solution where the gradient necessarily becomes small. It is however, very robust.

The Gauss–Newton method is a modification of Newton's method which is very fast near the solution. The Gauss–Newton method compared to the Newton's method has the advantage that the second derivative of J, which can be challenging to compute, is not required.

The second derivative $\mathbf{J}''$ is calculated only once, after the process of the Levenberg-Marquardt algorithm, to compute the output uncertainties.

The Levenberg-Marquardt inversion algorithm starts with an initialisation to set the cost at the first guess state (see Section 4.3.2.2), $J(\mathbf{x}_0)$, and, normally, to set the initial state for the iteration equal to the first guess, $\mathbf{x}_n = \mathbf{x}_0$.

A maximum number of iterations is permitted, and if no convergence is reached after this number, the algorithm exits at the current state (the iteration count is part of the standard output of the CISAR so that this exit condition can be checked in the results).

4.3.2.4 Convergence criteria The iteration process is stopped when the decrease in J between iterations, δJ_n is so small as to be negligible or when the number of iterations reaches a maximum threshold defined at the begining of the inversion.

4.3.3 Quality Indicator

The Quality Indicator provides an indication on the reliability of the retrieved solution. This Quality Indicator depends on several factors depending on the sensitivity of the state variable to the observed signal and to the efficiency of the inversion process. The following parameters are considered for the quality control:

1. **Convervenge**: whether the inversion has reached the maximum number of iterations or not.
2. **Entropy RPV** : the entropy quantifies the information coming from the observation. The entropy for the RPV parameters is calculated as follow:
$$H = -\frac{1}{2} ln \left(\frac{\sigma_{post}}{\sigma_{prior}} \right) \tag{59}$$
where σ_{post} is the uncertainty of the solution and σ_{prior} is the uncertainty of the prior information.
3. **Entropy AOT** : same as above but for the AOT.
4. **AOT Jacobian** : it gives information on the dependency of the forward model on the aerosol optical thickness. The magnitude of the Jacobian is weighted by the observation uncertainty.
5. **Residuals** : residuals of the observation term of the cost function.

For each of these fields a test is designed a quality q_i is assigned. For the convergence $q_i = 0$ when the maximum number of iteration is reached and $q_i = 1$ otherwise. For all the other fields two thresholds T_1 and T_2 are defined. The following equation is then analysed:

$$s_i T_{i1} \leq p_i(t) \leq s_i T_{i2} \tag{60}$$

where $p_i(t)$ is the value of the parameter p_i for the observation t.When p_i is lower than $s_i T_{i1}$ the corresponding quality q_i is set to 0. When p_i is higher than $s_i T_{i1}$ a quality q_i of 1 is given. When p_i falls within the $[s_i T_{i1}, s_i T_{i2}$ interval, a non-linear model is used to define the test value q_i and range between m_i and 1, where m_i is the minimum value assigned to q_i, allowing to give minimum weight to the different tests.

When all the tests have been performend, the final quality indicator (QI) is computed as follows:

$$\begin{cases} QI = 0, & \text{if } \sum_i (1 - q_i) \geq 1. \\ QI = 1 - \sum_i (1 i q_i) \geq 1, & \text{otherwise.} \end{cases} \tag{61}$$

where i=2,..,5.

4.3.4 Linear error analysis

The retrieval uncertainty is based on the OE theory, assuming a linear behaviour of $y(\mathbf{x}, \mathbf{b})$ in the vicinity of the solution $\hat{\mathbf{x}}$. Under this condition, the retrieval uncertainty $\sigma_{\hat{\mathbf{x}}}$ is determined by the shape of $J(\mathbf{x})$ in $\hat{\mathbf{x}}$

$$\sigma_{\hat{\mathbf{x}}}^2 = \left(\frac{\partial^2 J(\mathbf{x})}{\partial \mathbf{x}^2} \right)^{-1} = \left(\mathbf{K}_x^T \, \mathbf{S}_y^{-1} \, \mathbf{K}_x + \mathbf{S}_x^{-1} + \hat{\mathbf{S}}_a + \hat{\mathbf{S}}_l \right)^{-1} \tag{62}$$

where $\mathbf{K}_x$ is the gradient of $y(\mathbf{x}, \mathbf{b})$ calculated in $\hat{\mathbf{x}}$. The uncertainty $\sigma_{\hat{\mathbf{x}}}^2$ is actually composed of two distinct contributions:

- **Null space uncertainty** This uncertainty is given by

$$\mathbf{S}_N = (\mathbf{D}_y \mathbf{K}_x - \mathbf{m}) \, \mathbf{S}_s \, (\mathbf{D}_y \mathbf{K}_x - \mathbf{m}) \tag{63}$$

  where $\mathbf{D}_y$ is the inverse operator $\mathbf{D}_y = \partial \hat{\mathbf{x}} / \partial y_m$

$$\mathbf{D}_y = \left(\mathbf{K}_x^T \, \mathbf{S}_y^{-1} \, \mathbf{K}_x + \mathbf{S}_x^{-1} + \hat{\mathbf{S}}_a + \hat{\mathbf{S}}_l \right)^{-1} \mathbf{K}_x^T \, \mathbf{S}_y^{-1} \tag{64}$$

  $\mathbf{S}_N$ expresses the uncertainty that arises from a basic lack of information in the measurement system.

- **Measurement uncertainty** This uncertainty is given by

$$\mathbf{S}_M = \mathbf{D}_y \, \mathbf{S}_y \, \mathbf{D}_y^T \tag{65}$$

  The model parameter uncertainty is included into the measurement uncertainty.

4.4 Product generation

The inversion process provides the solution vector $\hat{\mathbf{x}}$ that minimizes the cost function J. This solution vector includes for each spectral band $\tilde{\lambda}$ the retrieved value of the RPV parameters $(\hat{\rho}_0(\tilde{\lambda}), \hat{k}(\tilde{\lambda}), \hat{\Theta}(\tilde{\lambda}), \hat{h}(\tilde{\lambda}))$ and associated estimated uncertainty $(\sigma_{\hat{\rho}_0}, \sigma_{\hat{k}}, \sigma_{\hat{\Theta}}, \sigma_{\hat{h}})$.from these parameters, it is possible to estimate the isotropic BiHemispherical Reflectance (BHR) or white sky albedo. $BHR_\bullet(\tilde{\lambda})$ represents the surface albedo that would be observed in band $\tilde{\lambda}$ under perfectly isotropic illumination conditions. It writes

$$BHR_\bullet(\tilde{\lambda}) = \rho_0(\tilde{\lambda}) \, \frac{1}{4\pi} \int_{\pi/2} \int_{2\pi} \breve{\rho}_s(k(\tilde{\lambda}), \Theta(\tilde{\lambda}), h(\tilde{\lambda}); \mu_0, -\mu_v, \phi_r) \, d\Omega_v \, d\Omega_s \tag{66}$$

The corresponding error uncertainty writes

$$\sigma_{BHR_\bullet}(\tilde{\lambda}) = \sqrt{\sum_{i=1}^{4} \left(\frac{\partial BHR_\bullet(\tilde{\lambda})}{\partial x_i} \, \sigma_{x_i}(\tilde{\lambda}) \right)^2} \tag{67}$$

where x_i are the RPV parameters and $\sigma_{\hat{x}_i}(\tilde{\lambda})$ the estimated uncertainty of parameter $\hat{x}_i$ in band $\tilde{\lambda}$.

5 ASSUMPTIONS AND LIMITATIONS

5.1 Assumptions

The CISAR algorithm relies on the following assumptions:

1. Satellite observations are unbiased with an uncertainty characterised by a Gaussian distribution.
2. The radiation regime at the spatial scale of a PROBA-V pixel can be represented with a one dimensional horizontally homogeneous RTM.
3. Topography and slope effects are ignored, *i.e.*, pixels are assumed flat.
4. A limited number of aerosol classes can be used to describe the spectral variability of their properties.
5. The surface radiative properties do not change during the course of the accumulation period.
6. The RPV model is considered adequate to accurately represent all types of surface BRF everywhere and all year long at the spatial scale of a PROBA-V pixel;

5.2 Limitations

The following limitations apply to the CISAR algorithm:

1. PROBA-V observations are processed only of the corresponding Sun and observation zenith angles are less than 70°.
2. No retrieval will take place if the number of PROBA-V observations per channel is smaller than $4 + N_a + 1$ where N_a is the number of aerosol classes.

6 Input data requirements

6.1 Setup parameters

The following main run-time setup parameters are used within CISAR :

Symbol	**Description**	Default value
	Maximum number of iterations	60
$\theta_{\max}$	Maximum processed sun and viewing zenith angles	70°
A_a	Coefficient of Equation (34)	0.25
A_b	Coefficient of Equation (34)	1.2
A_c	Coefficient of Equation (34)	7.00
N_d	Duration in day of the accumulation period	16
N_s	Duration in day of the shift between two accumulation periods	8
σ_L	Uncertainty on AOT spectral relationship defined in Section (4.2.3.5)	1.0
$\sigma_{\min}$	Minimum error on the surface parameters	0.15
τ_{low}	Minimum AOT first guess value	0.0001
τ_{high}	Maximum AOT first guess value	0.4

6.2 PROBA-V TOA BRF

Level 1b PROBA-V TOA BRF $\mathbf{y}(t, \tilde{\lambda}, \mathbf{p})$ as given by Equation (19) is the main input required by the CISAR algorithm. In addition to the TOA BRF, the following information is required :

Field	**Variable**	**DESCRIPTION**
TOABRF	$\mathbf{y}(t, \tilde{\lambda}, \mathbf{p})$	Level 2A PROBA-V TOA BRF
TIME	t	Acquisition time
RADNOISE	$\sigma_i(\tilde{\lambda})$	Radiometric noise in each spectral band $\tilde{\lambda}$
NAVSIGX	$\sigma_x(\tilde{\lambda})$	E-W navigation uncertainty of band $\tilde{\lambda}$
NAVSIGY	$\sigma_y(\tilde{\lambda})$	N-S navigation uncertainty of band $\tilde{\lambda}$
LAT		Pixel latitude
LON		Pixel longitude

6.3 Ancillary information

The following ancillary information is requested:

Data	Type	Unit	Description
CMa	Dynamic	N/A	Cloud mask provided from PROBA-V input data
TCWV	Dynamic	kg/m^2	Total column water vapour taken from ECMWF reanalysis data, linearly interpolated in time, bilinearly in space
TCO3	Dynamic	Dobson	Total column ozone taken from ECMWF reanalysis data, linearly interpolated in time, bilinearly in space
SRFP	Dynamic	hPa	Surface pressure taken from ECMWF reanalysis data. Surface pressure is calculated from a standard value of 1013.25 hPa at sea level and is converted to pressure at a certain height, using a conversion formula of Plummer et al. (2003).
SWS	Dynamic	m/s	Surface wind speed taken from ECMWF reanalysis data.
h	Dynamic	km	Monthly aerosol layer height.
LSM	Static	N/A	Land-sea mask
EVL	Static	m	Pixel elevation

Dynamic data are updated for each processed L1b image. Static data are computed once and for all.

6.4 Product data output format

Currently, the CISAR algorithm is only applied over AERONET stations. It processes PROBA-V level 1b data extracted over these stations. The extracted period runs from 01/01/2014 to 31/12/2015.

One NetCDF file is generated per stations and contains the results of the inversion for the entire extracted year. These product data files are named according to the following convention

`CISAR_TTarget_PYYYYMMDD_yyyymmdd.nc`

where

`Target` is the name of the processed target
`YYYY` is the year of the first day of the processed period
`MM` is the month of the first day of the processed period
`DD` is the day of the first day of the processed period
`yyyy` is the year of the last day of the processed period
`mm` is the month of the last day of the processed period
`dd` is the day of the last day of the processed period

One product NetCDF result file contains the following fields:

Field name	Symbol	Eq.	Description
acquisition_time			
rho_0	$\hat{\rho}_0(\tilde{\lambda})$	46	Retrieved $\hat{\rho}_0(\tilde{\lambda})$ value in the four PROBA-V bands
k	$\hat{k}(\tilde{\lambda})$	46	Retrieved $\hat{k}(\tilde{\lambda})$ value in the four PROBA-V bands
theta	$\hat{\Theta}(\tilde{\lambda})$	46	Retrieved $\hat{\Theta}(\tilde{\lambda})$ value in the four PROBA-V bands
h	$\hat{h}(\tilde{\lambda})$	46	Retrieved $\hat{h}(\tilde{\lambda})$ value in the four PROBA-V bands
sigma_rho_0	$\sigma_{\hat{\rho}_0}(\tilde{\lambda})$	62	Estimated uncertainty $\sigma_{\hat{\rho}_0}(\tilde{\lambda})$ in the four PROBA-V bands
sigma_k	$\sigma_{\hat{k}}(\tilde{\lambda})$	62	Estimated uncertainty $\sigma_{\hat{k}}(\tilde{\lambda})$ in the four PROBA-V bands
sigma_theta	$\sigma_{\hat{\Theta}}(\tilde{\lambda})$	62	Estimated uncertainty $\sigma_{\hat{\Theta}}(\tilde{\lambda})$ in the four PROBA-V bands
sigma_h	$\sigma_{\hat{h}}(\tilde{\lambda})$	62	Estimated uncertainty $\sigma_{\hat{h}}(\tilde{\lambda})$ in the four PROBA-V bands
bhr	$BHR_{\bullet}(\tilde{\lambda})$	66	Calculated $BHR_{\bullet}$ in the four PROBA-V bands
sigma_bhr	$\sigma_{BHR_{\bullet}}(\tilde{\lambda})$	67	Estimated $BHR_{\bullet}$ uncertainty in the four PROBA-V bands
aot_fine_550			
aot_coarse_550			
aot_total_550	$\hat{\tau}_a(0.55)$	46	Total aerosol optical thickness in layer L_a at 0.55μm
sigma_aot_fine_550			
sigma_aot_coarse_550			
sigma_aot_total_550	$\sigma_{\hat{\tau}_a}(0.55)$	62	Estimated aerosol optical thickness uncertainty in layer L_a at 0.55μm
start_period			
end_period			
QI			Quality Indicator
quality_information			Results of the tests performed on the parameter to define the QI

7 ALGORITHM IMPLEMENTATION

This section contains some practical information concerning the implementation of the CISAR algorithm.

7.1 Input data preparation

In this phase the input data are prepared for each target. The radiometric noise is calculated for each band and the ancillary information are retrieved.

7.2 Overall CISAR data flow

The overall CISAR data flow is presented in Figure (6). The processing is composed of three major steps:

1. **INPUT DATA PREPARATION** In this module, PROBA-V TOA BRF values are accumulated during N_d days together with all the ancillary information listed in Section (6.3). It also load the prior information which is set to climatological background values when the first accumulation period is processed.
2. **INVERSION** At the end of the input data preparation, the inversion process takes place for each accumulation period. The solutions and associated uncertainties are stored in disk files. The prior information on the state of the surface is updated.
3. **PRODUCT GENERATION** When all the accumulation periods are processed, one NetCDF file described in Section (4.4) is generated.

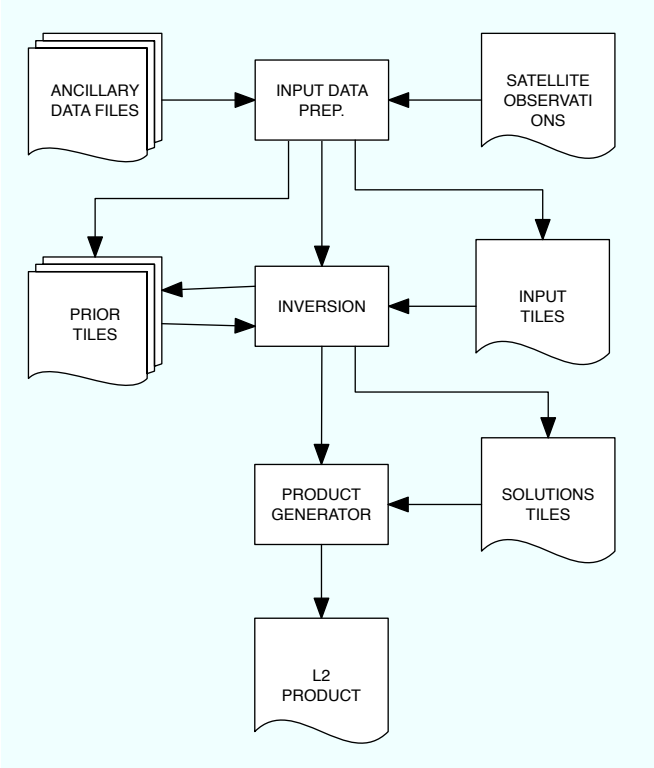

Figure 6: Overall data flow for the processing of PROBA-V data. The external data files are the files containing the ancillary information necessary to prepare the input files, together with the satellite data. When all the input files are prepared the inversion takes place. At the end of the inversion the prior is updated and the solution uncertainty estimated. The solutions and the relative uncertainties are finally combined to generate a single product.

References

Cox, C. and W. Munk (1954, November). Measurement of the Roughness of the Sea Surface from Photographs of the Sun's Glitter. Journal of the Optical Society of America 44(11), 838–850.

Diner, D. J., J. V. Martonchik, R. A. Kahn, B. Pinty, N. Gobron, D. L. Nelson, and B. N. Holben (2005). Using angular and spectral shape similarity constraints to improve {MISR} aerosol and surface retrievals over land. Remote Sensing of Environment 94, 155–171.

Dubovik, O., M. Herman, A. Holdak, T. Lapyonok, D. Tanré, J. L. Deuzé, F. Ducos, A. Sinyuk, and A. Lopatin (2011). Statistically optimized inversion algorithm for enhanced retrieval of aerosol properties from spectral multi-angle polarimetric satellite observations. Atmospheric Measurement Techniques 4, 975–1018.

Dubovik, O., A. Sinyuk, T. Lapyonok, B. N. Holben, M. Mishchenko, P. Yang, T. F. Eck, H. Volten, O. Munoz, B. Veihelmann, W. J. van der Zande, J. F. Leon, M. Sorokin, and I. Slutsker (2006). Application of spheroid models to account for aerosol particle nonsphericity in remote sensing of desert dust. Journal of Geophysical Research-Atmospheres 111(D11), 11208–11208.

Engelsen, O., B. Pinty, M. M. Verstraete, and J. V. Martonchik (1996). Parametric bidirectional reflectance factor models: evaluation, improvements and applications.

Fischer, J. and H. Grassl (1984). Radiative transfer in an atmosphere-ocean system: an azimuthally dependent matrix-operator approach. Applied Optics 23, 1032–1039.

Govaerts, Y. and M. Luffarelli (2017, March). Joint retrieval of surface reflectance and aerosol properties with continuous variations of the state variables in the solution space: Part 1: theoretical concept. Atmos. Meas. Tech. Discuss. 2017, 1–27.

Govaerts, Y. M., S. Wagner, A. Lattanzio, and P. Watts (2010, January). Joint retrieval of surface reflectance and aerosol optical depth from MSG/SEVIRI observations with an optimal estimation approach: 1. Theory. Journal of Geophysical Research 115(D02203), doi:10.1029/2009JD011779.

Kinne, S., D. O'Donnel, P. Stier, S. Kloster, K. Zhang, H. Schmidt, S. Rast, M. Giorgetta, T. F. Eck, and B. Stevens (2013, December). MAC-v1: A new global aerosol climatology for climate studies. Journal of Advances in Modeling Earth Systems 5(4), 704–740.

Koepke, P. (1984, June). Effective reflectance of oceanic whitecaps. Applied Optics 23(11), 1816.

Liu, Q. and E. Ruprecht (1996). Radiative transfer model: matrix operator method. Applied Optics 35, 4229–4237.

Morel, A. (1988, September). Optical modeling of the upper ocean in relation to its biogenous matter content (case I waters). Journal of Geophysical Research: Oceans 93(C9), 10749–10768.

Plummer, S., J. Chen, G. Dedieu, and M. Simon (2003). GLOBCARBON Detailed Processing Model. Technical Report GLBC-ESL-DPM-V1.3.

Rahman, H., B. Pinty, and M. M. Verstraete (1993). Coupled surface-atmosphere reflectance (CSAR) model. 2. Semiempirical surface model usable with NOAA Advanced Very High Resolution Radiometer Data. Journal of Geophysical Research 98(D11), 20,791–20,801.

Rodgers, C. D. (2000). Inverse methods for atmospheric sounding. Series on Atmospheric Oceanic and Planetary Physics. World Scientific.

Sterckx, S., I. Benhadj, G. Duhoux, S. Livens, W. Dierckx, E. Goor, S. Adriaensen, W. Heyns, K. Van Hoof, G. Strackx, K. Nackaerts, I. Reusen, T. Van Achteren, J. Dries, T. Van Roey, K. Mellab, R. Duca, and J. Zender (2014, April). The PROBA-V mission: image processing and calibration. International Journal of Remote Sensing 35, 2565–2588.

Vermote, E. F., D. Tanre, J. L. Deuze, M. Herman, and J. J. Morcrette (1997). Second simulation of the satellite signal in the solar spectrum, 6s: An overview. IEEE TGARS 35(3), 675–686.

Wiscombe, W. J. (1977). The Delta-M Method: Rapid Yet Accurate Radiative Flux Calculations for Strongly Asymmetric Phase Functions. Journal of Atmospheric Sciences 34, 1408–1422.